Full-wave simulations of ICRF heating regimes in toroidal plasma with non-Maxwellian distribution functions

Global-wave solutions in ion cyclotron heated plasmas
E.F. Jaeger, R.W. Harvey, L.A. Berry et al.

Nonthermal particle and full-wave diffraction simulations
J.C. Wright, L.A. Berry, P.T. Bonoli et al.

A model for self-consistent simulation of ICRH suitable for integrating modelling
T. Hellsten, A. Hannan, T. Johnson et al.

Advances in numerical simulations of ion cyclotron heating
M. Brambilla and R. Bilato

Benchmarking ICRF full-wave solvers for ITER
R.V. Budny, L. Berry, R. Bilato et al.

Poloidal asymmetries due to ion cyclotron resonance heating
Ye O Kazakov, I Pusztai, T Fülöp et al.

A description of the full-particle-orbit-following SPIRAL code for simulating fast-ion experiments in tokamaks
G J Kramer, R V Budny, A Bortolon et al.

Energetic particle physics in fusion research in preparation for burning plasma experiments
N.N. Gorelenkov, S.D. Pinches and K. Toi

On radio frequency current drive in the ion cyclotron range of frequencies in DEMO and large ignited plasmas
Marco Brambilla and Roberto Bilato

Full-wave simulations of ICRF heating regimes in toroidal plasma with non-Maxwellian distribution functions

N. Bertelli[1], E.J. Valeo[1], D.L. Green[2], M. Gorelenkova[1], C.K. Phillips[1], M. Podestà[1], J.P. Lee[3], J.C. Wright[3] and E.F. Jaeger[4]

[1] Princeton Plasma Physics Laboratory, Princeton, NJ 08543, United States of America
[2] Oak Ridge National Laboratory, PO Box 2008, Oak Ridge, TN 37831-6169, United States of America
[3] Plasma Science and Fusion Center, MIT, Cambridge, MA 02139, United States of America
[4] XCEL Engineering Inc., 1066 Commerce Park Drive, Oak Ridge, TN 37830, United States of America

E-mail: nbertell@pppl.gov

Abstract

At the power levels required for significant heating and current drive in magnetically-confined toroidal plasma, modification of the particle distribution function from a Maxwellian shape is likely (Stix 1975 *Nucl. Fusion* **15** 737), with consequent changes in wave propagation and in the location and amount of absorption. In order to study these effects computationally, both the finite-Larmor-radius and the high-harmonic fast wave (HHFW), versions of the full-wave, hot-plasma toroidal simulation code TORIC (Brambilla 1999 *Plasma Phys. Control. Fusion* **41** 1 and Brambilla 2002 *Plasma Phys. Control. Fusion* **44** 2423), have been extended to allow the prescription of arbitrary velocity distributions of the form $f(v_\parallel, v_\perp, \psi, \theta)$. For hydrogen (H) minority heating of a deuterium (D) plasma with anisotropic Maxwellian H distributions, the fractional H absorption varies significantly with changes in parallel temperature but is essentially independent of perpendicular temperature. On the other hand, for HHFW regime with anisotropic Maxwellian fast ion distribution, the fractional beam ion absorption varies mainly with changes in the perpendicular temperature. The evaluation of the wave-field and power absorption, through the full wave solver, with the ion distribution function provided by either a Monte-Carlo particle and Fokker–Planck codes is also examined for Alcator C-Mod and NSTX plasmas. Non-Maxwellian effects generally tend to increase the absorption with respect to the equivalent Maxwellian distribution.

Keywords: tokamak, ICRH, waves, plasma, HHFW, minority heating

(Some figures may appear in colour only in the online journal)

1. Introduction

The injection of waves in the ion cyclotron frequency range is a well-established method of heating and driving current in magnetically confined toroidal plasma. A straightforward estimate suggests that, at RF power levels which are sufficiently high that finite enhancements in temperature or current are achieved, the ion velocity distribution functions are expected to be significantly modified from a thermal, Maxwellian shape [1]. Since the absorption of energy and momentum are mainly through collisionless wave-particle interactions, local in velocity space, these distribution function modifications will, generally, result in finite changes in the amount and spatial location of absorption. Inclusion of these modifications, ultimately computed self-consistently together with the wave fields, is required to more faithfully model experimental results and to more accurately design future devices.

There has been substantial progress recently to address these considerations. More recently, the all-orders (in Larmor radius to wavelength) global-wave solver AORSA [2] has been

coupled to the CQL3D Fokker–Planck code [3, 4]. The combination has been iteratively solved to self-consistently compute wave-fields and ion distribution functions [5]. Similar work has been done with other RF numerical tools, such as METS [6, 7], GNET-TASK/WM [8], SSPQL/TORIC v.6 package [9, 10], CYRANO [11] ORBIT-RF/AORSA [12], VENUS-LEMan in the SCENIC package [13], EVE [14, 15], and SELFO-light [16].

Here, we describe the extension of both the finite Larmor radius (FLR) and the high harmonic fast wave (HHFW) versions of the TORIC code [17, 18] to include non-Maxwellian distribution functions. The version of TORIC used in this work corresponds to the TORIC's version also named TORIC v.5 and currently implemented in the TRANSP code [19]. Indeed, this work is a starting point to be able to treat self-consistently in TRANSP the evolution of the H minority and beam ion population in the presence of RF heating. As mentioned above, there are two versions of the code: (i) FLR and (ii) HHFW regimes. The former makes use of the assumption that the ion Larmor radius ρ_i is small-but-finite compared to the scale of wave field variation perpendicular to the local magnetic field direction, $\hat{\mathbf{b}}$, i.e. $\rho_i |\hat{\mathbf{b}} \times \nabla A/A| \ll 1$, for any field component A. This approximation greatly reduces the computational burden while still accurately reproducing results obtained from the more general codes when the small-Larmor-radius approximation is verified *a posteriori*. More specifically, TORIC takes into account FLR corrections only up to $\omega = 2\,\Omega_{c,i}$ (where ω and $\Omega_{c,i}$ are the angular frequency and the ion cyclotron angular frequency, respectively). On the other hand, in the HHFW version of the code, coefficients of the wave equation are replaced by the corresponding elements of the full hot-plasma dielectric tensor where the k (k is the wave-vector) value in the argument of the Bessel functions is obtained by solving the local dispersion relation for the fast wave (FW) root.

The code extensions are presented in detail in section 2 together with a brief description of the code. The numerical implementation is presented in section 3. Results of applications are presented in section 4 for both isotropic and anisotropic distribution functions in Alcator C-Mod [20] and NSTX [21] plasmas. Finally, a discussion and the main conclusions of the work are summarized in section 5.

2. Code description

2.1. The finite-Larmor-radius full-wave TORIC version

The TORIC code solves the vector wave equation

$$\nabla \times \nabla \times \mathbf{E} = \frac{\omega^2}{c^2}\left[\mathbf{E} + \frac{4\pi i}{\omega}(\mathbf{J}^P + \mathbf{J}^A)\right] \quad (1)$$

for the vector electric field $\mathbf{E}$ (assuming a harmonic dependence on time, namely, $E \propto e^{(-i\omega t)}$). The undriven plasma is assumed time independent and toroidally symmetric. Therefore, the response to a prescribed antenna current density $\mathbf{J}^A(\mathbf{x}_p, \phi, t)$ as a function of poloidal position $\mathbf{x}_p$, toroidal angle ϕ, and time

t, can be obtained by summation of responses to each Fourier component $\mathbf{J}^A(\mathbf{x}_p, n_\phi, \omega)\exp[i(n_\phi\phi - \omega t)]$ with frequency ω and toroidal mode number n_ϕ. The plasma current density $\mathbf{J}^P$,

$$\mathbf{J}^P \equiv \sum_s q_s \int d\mathbf{v}\, \mathbf{v} f_s(\mathbf{x}, \mathbf{v}; \omega) \quad (2)$$

requires the solution for the particle distribution functions $f_s(\mathbf{x}, \mathbf{v}; \omega)$, for each species s, which is computed by solving the linearized Vlasov equation with several assumptions: the particle gyro-radii are small compared to the scale of field variation perpendicular to the local magnetic field direction, $\mathbf{b} \equiv \mathbf{B}/|\mathbf{B}|$; the effects of drifts across the magnetic flux surfaces are negligible; multiple resonant wave-particle interactions are uncorrelated. The small-Larmor-radius approximation reduces the response to cross-field variations of $\mathbf{E}$ from an integral to a differential form. Spatial dependence is further decomposed into variation within and across poloidal flux surfaces, $\psi(\mathbf{x}) = \text{const.}$ Fourier decomposition of variation within surfaces,

$$A(r, z) = \sum_m A_m(\psi)\, e^{im\theta} \quad (3)$$

and projection of the wave equation onto test functions $\mathbf{F}(\psi)$ with compact support transforms the system into a dense block (in m)—tridiagonal (in ψ) system which is soluble using standard numerical methods. By virtue of this decomposition, the local parallel component of the wave-vector is explicitly represented as

$$k_\parallel(\theta, \psi) \equiv \mathbf{k} \cdot \mathbf{b} = (m\nabla\theta + n_\phi\nabla\phi) \cdot \mathbf{b}. \quad (4)$$

This representation facilitates the required computation of the elements of the local susceptibility tensor χ_s relating the current $\mathbf{J}_s^P$ in species s, to the driving electric field

$$\mathbf{J}_s^P = -\frac{i\omega}{4\pi}\chi_s \cdot \mathbf{E}. \quad (5)$$

In the original version of TORIC code, the elements of the local susceptibility tensor χ_s are restricted to the Maxwellian case. Here, following the derivation and notation of [17, 22], we generalize the essential terms $(\hat{R}, \hat{L}, \rho^{(2)}, \lambda^{(2)})$ originally implemented in the IC minority version of TORIC for arbitrary velocity distribution functions of the form $f_s(\mathbf{v}) = f_s(v_\perp, v_\parallel)$:

$$\begin{pmatrix}\hat{R}\\ \hat{L}\end{pmatrix} = 1 + \sum_s \frac{\omega_{ps}^2}{\omega}\begin{pmatrix}A_{-1,0}\\ A_{1,0}\end{pmatrix}, \quad (6)$$

and

$$\begin{pmatrix}\hat{\rho}^{(2)}\\ \hat{\lambda}^{(2)}\end{pmatrix} = -\frac{1}{2}\sum_s \frac{\omega_{ps}^2}{\omega_{cs}^2}\frac{w_\perp^2}{c^2}\begin{pmatrix}\omega A_{-2,1}\\ \omega A_{2,1}\end{pmatrix}, \quad (7)$$

where the coefficients A are

$$A_{n,j} = \int_{-\infty}^{\infty} dv_\parallel \frac{1}{\omega - k_\parallel v_\parallel - n\,\Omega_c}$$
$$\times \int_0^{+\infty} 2\pi v_\perp dv_\perp H_j(v_\parallel, v_\perp) \quad (8)$$

for $j = 0, 1$, with

$$H_0(v_\parallel, v_\perp) = \frac{1}{2}\frac{k_\parallel w_\perp^2}{\omega}\frac{\partial f_0}{\partial v_\parallel} - \left(1 - \frac{k_\parallel v_\parallel}{\omega}\right)f_0(v_\parallel, v_\perp)$$

$$H_1(v_\parallel, v_\perp) = \frac{1}{4}\frac{k_\parallel w_\perp^2}{\omega}\frac{\partial f_0}{\partial v_\parallel}\frac{v_\perp^4}{w_\perp^4}$$
$$- \left(1 - \frac{k_\parallel v_\parallel}{\omega}\right)f_0(v_\parallel, v_\perp)\frac{v_\perp^2}{w_\perp^2}. \tag{9}$$

and

$$w_\perp^2 \equiv \int_{-\infty}^{\infty}\mathrm{d}v_\parallel\int_0^{+\infty}2\pi v_\perp\mathrm{d}v_\perp v_\perp^2 f_0(v_\parallel, v_\perp). \tag{10}$$

The derivation of these equations is based on the generalization of the plasma dielectric tensor for non-Maxwellian distributions in the FLR limit shown in [23]. Equations (6) and (7) have been implemented in the new code extension (see section 3) in order to deal with arbitrary distribution functions and its applications are shown in section 4.

2.2. The high-harmonic fast wave full-wave `TORIC` version

The HHFW version of the code makes use of the so-called 'Quasi-local' approximation (see details in [18]). The 0th-order FLR coefficients of the wave equation are replaced by the corresponding elements of the full hot-plasma dielectric tensor in which the k^2 value in the argument of the Bessel functions is obtained by solving the local dispersion relation for FWs. At each point the resulting wave equation, which is still in differential form along the radial coordinate, has the same dispersion relation as the full integral wave equation, although only for FWs.

Similarly to the FLR case described above, the extensions of HHFW version consists mainly in the implementation of the full-hot susceptibility tensor χ for arbitrary velocity distribution functions instead of the original implementation which was restricted to the Maxwellian case. In particular, the elements of the local susceptibility tensor χ for arbitrary velocity distribution functions are of the form [24]

$$\chi_s = \frac{\omega_{ps}^2}{\omega}\int_0^{+\infty}2\pi v_\perp\mathrm{d}v_\perp$$
$$\times \int_{-\infty}^{+\infty}\mathrm{d}v_\parallel\hat{\mathbf{z}}\hat{\mathbf{z}}\frac{v_\parallel^2}{\omega}\left(\frac{1}{v_\parallel}\frac{\partial f}{\partial v_\parallel} - \frac{1}{v_\perp}\frac{\partial f}{\partial v_\perp}\right)_s$$
$$+ \frac{\omega_{ps}^2}{\omega}\int_0^{+\infty}2\pi v_\perp\mathrm{d}v_\perp$$
$$\times \int_{-\infty}^{+\infty}\mathrm{d}v_\parallel\sum_{n=-\infty}^{+\infty}\left[\frac{v_\perp U}{\omega - k_\parallel v_\parallel - n\Omega_{cs}}\mathbf{T}_n\right] \tag{11}$$

where

$$U \equiv \frac{\partial f}{\partial v_\perp} + \frac{k_\parallel}{\omega}\left(v_\perp\frac{\partial f}{\partial v_\parallel} - v_\parallel\frac{\partial f}{\partial v_\perp}\right) \tag{12}$$

and

$$\mathbf{T}_n = \begin{pmatrix} \dfrac{n^2 J_n^2(z)}{z^2} & \dfrac{inJ_n(z)J_n'(z)}{z} & \dfrac{nJ_n^2(z)v_\parallel}{zv_\perp} \\[3mm] -\dfrac{inJ_n(z)J_n'(z)}{z} & (J_n'(z))^2 & -\dfrac{iJ_n(z)J_n'(z)v_\parallel}{v_\perp} \\[3mm] \dfrac{nJ_n^2(z)v_\parallel}{zv_\perp} & \dfrac{iJ_n(z)J_n'(z)v_\parallel}{v_\perp} & \dfrac{J_n^2(z)v_\parallel^2}{v_\perp^2} \end{pmatrix},$$

with $z \equiv \frac{k_\perp v_\perp}{\Omega_{cs}}$.

3. Numerical implementation

The perpendicular velocity integrals produce smoothly varying functions of $v_\parallel$ whose product with the singular function $S = (\omega - k_\parallel v_\parallel - n\Omega)^{-1}$ must then be integrated in $v_\parallel$. For a non-drifting Maxwellian parallel-velocity distribution function with thermal velocity v_{th}, these integrals can be represented in terms of the plasma dispersion function $Z(\zeta/v_{th})$ [25] where $\zeta = (\omega - n\Omega)/k_\parallel$. For more general distributions, the integrations must be done numerically. Since these integrals are computed numerous times in forming the matrix system of field equations, efficient evaluation is essential. Further, since the co-factor of S is smooth, the resultant parallel integral's dependence on ζ will be smooth as well. We use this observation by evaluating the integrals at uniformly spaced points ζ_k and then interpolating the results to the desired value of ζ. Efficiency is gained by specifying the distribution function, and thus the co-factors, on the same, uniform, parallel velocity mesh, $v_k = k\,\Delta v$. Specifically, at a mesh point k, the integrals are of the form

$$I_k = \int\mathrm{d}v\frac{C(v)}{v - v_k}. \tag{13}$$

We approximate the cofactors

$$C(v) = \sum_j c_j T_j, \tag{14}$$

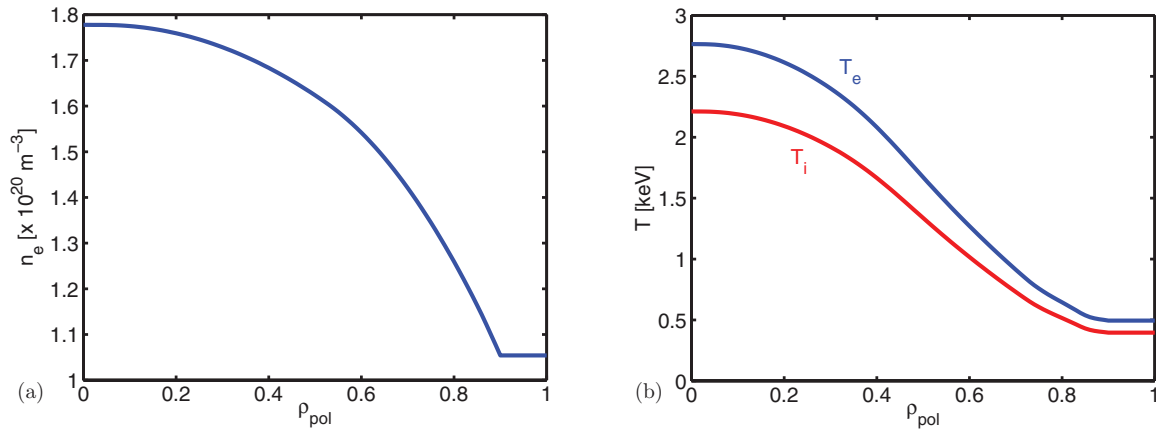where $c_j = C(v_j)$ and where T_j is a linear tent function surrounding v_j

$$T_j = \begin{cases} 1 - \dfrac{|v - v_j|}{\Delta v} & \text{if } |v - v_j| \leqslant \Delta v, \\[2mm] 0 & \text{otherwise.} \end{cases} \tag{15}$$
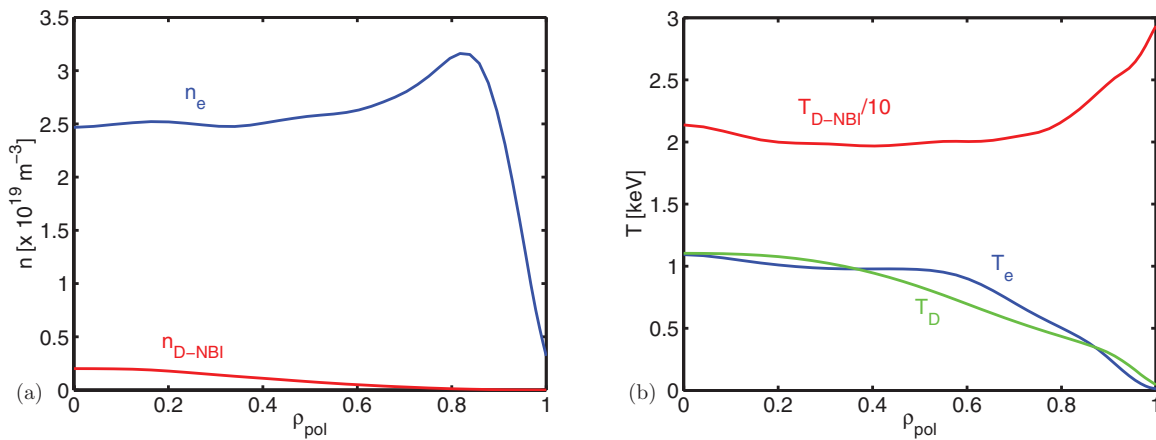
Then

$$I_k = \sum_j\int\mathrm{d}v\frac{c_j T_j}{v - v_k} = \sum_j c_j K_{j-k} = \sum c_{j+k}K_j. \tag{16}$$

where the kernel

$$K_j = \int_{-1}^1\mathrm{d}v\frac{1 - |v|}{v + j\Delta v}$$
$$= \begin{cases} \ln\left(\dfrac{j+1}{j-1}\right) - j\ln\left(\dfrac{j^2}{j^2 - 1}\right) & |j| > 1, \\[2mm] \pm\ln 4 & j = \pm 1, \\[2mm] i\pi & j = 0. \end{cases} \tag{17}$$

Figure 1. (*a*) The electron density profile, n_e as a function of the square root of the normalized poloidal flux, ρ_{pol} for an Alcator C-Mod plasma. (*b*) The electron and (common) ion temperature profiles as a function of ρ_{pol}.

Figure 2. (*a*) The electron density (n_e) and beam ion (n_{D-NBI}) profiles as a function of the square root of the normalized poloidal flux (ρ_{pol}) for an NSTX plasma. (*b*) The electron (T_e), thermal deuterium (T_D) and beam ion temperature (T_{D-NBI}) (rescaled by a factor 10) profiles as a function of ρ_{pol}.

The convolutions incur modest computational cost.

The approach described here has been originally used for the non-Maxwellian extension of the `TORIC` code in the lower hybrid frequency regime [26]. Furthermore, such method also motivated an improvement of the algorithm reducing the complexity from $\mathcal{O}(N^2)$ (which is what we use in this work) to $\mathcal{O}(N \log N)$, with N being the dimension of the core matrix [9, 27].

4. Applications

4.1. Parameters used when distribution function is provided by an analytical functional form

To validate the algorithm, calculations are presented of both minority hydrogen heating in a plasma equilibrium constructed from Alcator C-Mod tokamak data and HHFW heating regime in an NSTX plasma equilibrium. The electron density profile as a function of the square root of the normalized poloidal flux for the Alcator C-Mod discharge is shown in figure 1(*a*). The electron and ion temperature profiles are shown in figure 1(*b*). The corresponding plots for the NSTX plasma are shown in figure 2. The main parameters of these two machines are

Table 1. Toroidal field at magnetic axis (B_T), toroidal plasma current (I_p), magnetic axis major radius (R_0), wave frequency (f), and toroidal wave number (n_ϕ) for Alcator C-Mod and NSTX.

	B_T (T)	I_p (kA)	R_0 (cm)	f (MHz)	n_ϕ
Alcator C-Mod	5	627	68.26	78	10
NSTX	0.53	868	101.34	30	8

shown in table 1, indicating the toroidal field at magnetic axis (B_T), the toroidal plasma current (I_p), the magnetic axis major radius (R_0), the wave frequency (f), and the toroidal wave number (n_ϕ).

Moreover, for Alcator C-Mod case: the plasma consists of 7% fractional number density of hydrogen and 93% deuterium. For NSTX case: the plasma consists of 86.5% fractional number of density of (thermal) deuterium and 8% of beam deuterium (fast ions). An effective temperature of the beam ions (T_{bi}) given by [28]

$$T_{bi} = \frac{2}{3} \frac{u}{n_{bi}} \qquad (18)$$

is used. In equation (18) u and n_{bi} are the total energy density profile and the density of the beams ions, respectively, evaluated by `NUBEAM` [29, 30].
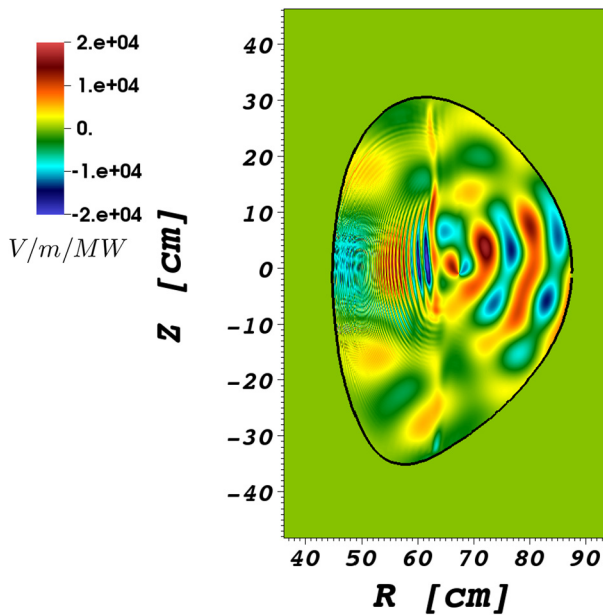
Figure 3. Real part of the right-handed wave electric field, Re(E_-), for an Alcator C-Mod plasma described in section 4.1.

4.2. Isotropic Maxwellian distributions

4.2.1. IC minority heating regime. The reference calculation assumes isotropic Maxwellian distributions, using the Z function to evaluate χ. Several qualitative features are clearly visible in the surface plot of Re(E_-), where $E^- \equiv E_x - iE_y$ (in Stix coordinates) shown in figure 3. The long wavelength fast wave, launched from the low-field side midplane is converted near the magnetic axis into a combination of moderate wavelength ion cyclotron waves (ICW, emanating rightward, toward the low field side) and short wavelength ion Bernstein waves (IBW, emanating leftward, toward the high field side). The relative power absorbed by second harmonic D, fundamental H and by the electrons for each wave branch is presented in table 2 in the column labeled 'Reference'. To check the accuracy of the method, the results were re-computed with the minority H susceptibility calculated numerically as described in section 3 for a Maxwellian distribution prescribed on a uniform numerical mesh of $N_{v_\parallel} = 500$ points and $N_{v_\perp} = 100$ points. The mesh range is $-c/100 \leqslant v_\parallel \leqslant c/100$ and $0 \leqslant v_\perp \leqslant c/100$ where $c = 3 \times 10^{10}$ cm s^{-1} is the speed of light. As shown in table 2, the power flow channels are well converged to the reference case with differences less than 1–2%. A more discriminating measure of convergence is shown in figure 4. Figure 4 shows the real part of the three components of the wave electric field (E_-, E_+, and $E_\parallel$) on the midplane both in high (left column) and low (right column) field regions. There, one can see an excellent agreement between the 'Reference' (solid (black) curve) and 'Numerical' (dashed (red) curve) cases.

Other cases with different resolutions in $v_\parallel$ and $v_\perp$ (not shown here) have been performed always obtaining an excellent agreement between reference and numerical cases in terms of electric field propagation, power density profiles, and total absorbed power.

Table 2. Alcator C-Mod: power flow to each species. The reference simulation corresponds to the original Maxwellian case while the numerical simulation numerically computed minority H susceptibility χ_H (equations (6)–(10)) assuming a Maxwellian functional form of the representation of the distribution function.

Absorbed fraction	Reference	Numerical
2nd Harmonic D	10.18%	10.28%
Fundamental H	69.95%	68.81%
Electrons—FW	11.35%	11.91%
Electrons—IBW	8.53%	9.00%

4.2.2. HHFW heating regime. Figure 5 shows the surface plot of Re(E_-) where the long wavelength fast wave is launched from the low-field side midplane. The relative power absorbed by D, fast ions (D-NBI), and electrons is presented in table 3 in the column labeled 'Reference'. As similarly done for IC minority heating regime, in order to assess the accuracy of the method, the results were re-computed with fast ions susceptibility calculated numerically as described in section 3 for a Maxwellian distribution prescribed on a uniform numerical mesh of $N_\parallel = 100$ points, $N_{v_\perp} = 50$ points, and $N_{N_\perp^2} = 35$. The mesh range is $-c/20 \leqslant v_\parallel \leqslant c/20$, $0 \leqslant v_\perp \leqslant c/20$, and $-3 \times 10^4 \leqslant N_\perp^2 \leqslant 9.5 \times 10^4$. Unlike the IC minority heating regime, the $N_\perp^2$ mesh has been added here to avoid multiple evaluations of the dispersion relation. As shown in table 3, the power flow channels are well converged to the reference case with differences less than 1%. Moreover, figure 6 shows the real part of the three components of the wave electric field (E_-, E_+, and $E_\parallel$) on the midplane both in high (left column) and low (right column) field sides. There, one can see an excellent agreement between the 'Reference' (solid (black) curve) and 'Numerical' (dashed (red) curve) cases.

As done in IC minority heating regime, other cases with different resolutions in $v_\parallel$, $v_\perp$ and $N_\perp^2$ (not shown here) have been performed always obtaining an excellent agreement between reference and numerical cases in terms of electric field propagation, power density profiles, and total absorbed power. These additional tests have also shown a smooth $N_\perp^2$ dependence of the components of χ, which allow us to decrease $N_{N_\perp^2}$ mesh points significantly reducing the computational time in evaluating the full hot plasma χ tensor.

4.3. Anisotropic Maxwellian distributions (bi-Maxwellian)

4.3.1. IC minority heating regime. The sensitivity of the principal absorption channel at the fundamental hydrogen resonance to changes in the shape of the hydrogen distribution was investigated by performing two series of computations, assuming an anisotropic Maxwellian form for the H distribution

$$f_H(v_\parallel, v_\perp) = (2\pi)^{-3/2}(v_{\text{th},\parallel}v_{\text{th},\perp}^2)^{-1}$$
$$\times \exp[-(v_\parallel/v_{\text{th},\parallel})^2 - (v_\perp/v_{\text{th},\perp})^2] \quad (19)$$

with $v_{\text{th},\parallel} = \sqrt{(2C_\parallel T(\psi)/m_H)}$,
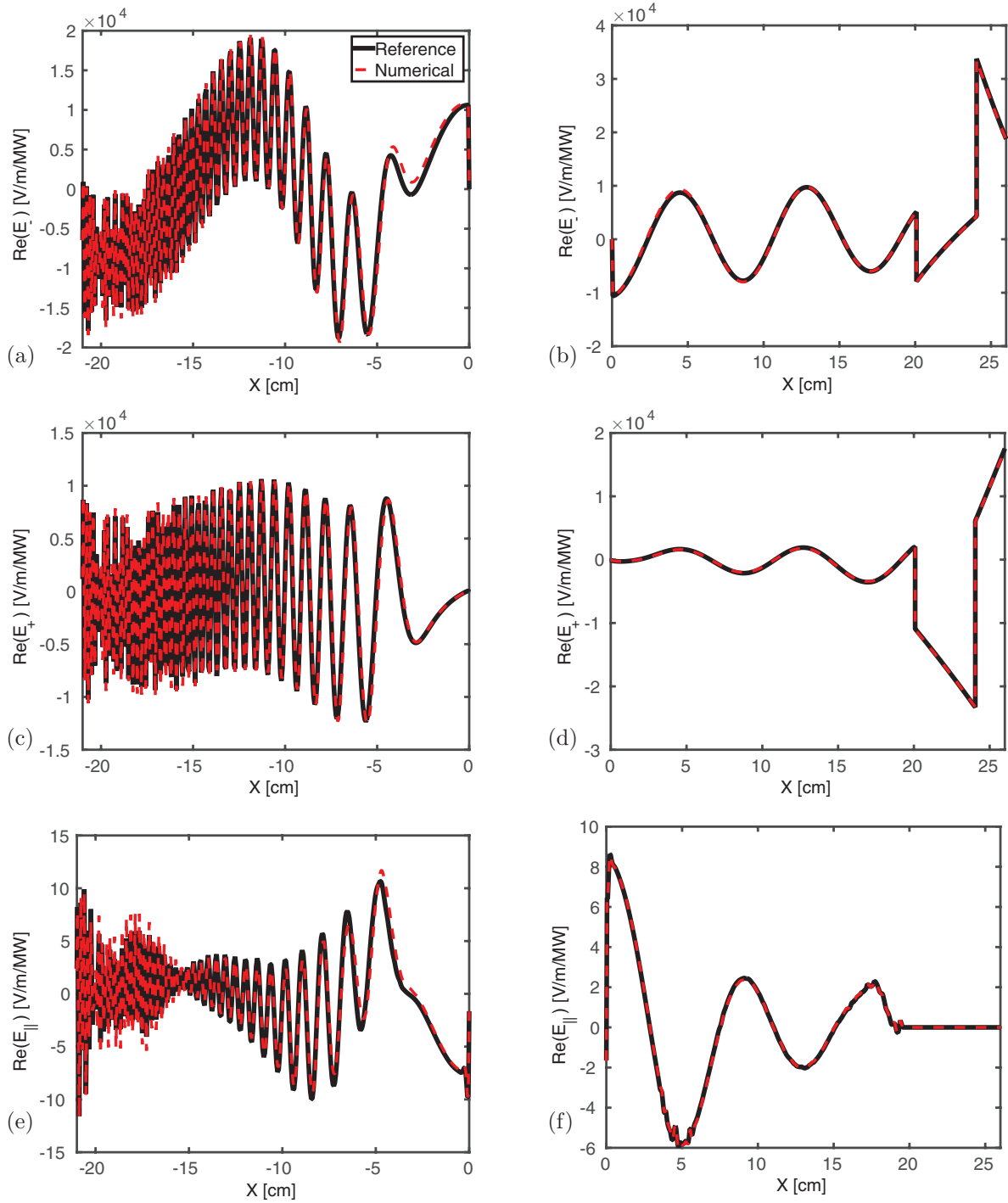
Figure 4. Figures (*a*) and (*b*): real part of the right-handed wave electric field, Re(E_-), both in the high field side region (figure (*a*)) and in the low field line region (figure (*b*)) on the midplane for an Alcator C-Mod plasma described in section 4.1. The solid (black) curve represents the 'Reference' case while the dashed (red) curve represents the results re-computed with the minority H susceptibility calculated numerically. Figures (*c*) and (*d*): real part of the left-handed wave electric field, Re(E_+), both in the high field side region (figure (*c*)) and in the low field line region (figure (*d*)). Figures (*e*) and (*f*): real part of the parallel wave electric field, Re($E_\parallel$), both in the high field side region (figure (*e*)) and in the low field line region (figure (*f*)).

$v_{\mathrm{th},\perp} = \sqrt{2C_\perp T(\psi)/m_H}$, with constants $C_\parallel$ and $C_\perp$ parameterizing the scans. The fundamental H absorption fraction, P_H varied by less than two percent when $C_\perp$ was varied from 0.5 to 5, with $C_\parallel$ held fixed at unity. In contrast the second series, in which $C_\perp$ was fixed at unity and $C_\parallel$ was varied showed a significant variation. For $C_\parallel = \{0.5, 1., 3., 5.\}$, the corresponding $P_H = \{61.27, 70.50, 90.46, 94.18\}$. In addition, while the absorption profile is localized to the resonant layer for small $C_\parallel$ it is significantly broadened radially at for large $C_\parallel$. This is clearly demonstrated in figure 7 where the absorption versus (*R,Z*) is shown for $C_\parallel = 0.5$ (figure 7(*a*)), $C_\parallel = 1.0$ (figure 7(*b*)), and $C_\parallel = 5.$ (figure 7(*c*)). Similar results and discussion are presented, for instance, in [31].
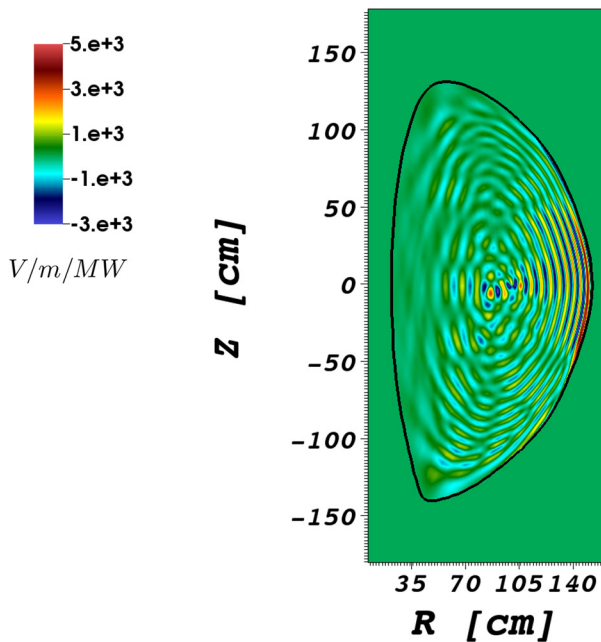
Figure 5. Real part of the right-handed wave electric field, Re(E_-), for an NSTX plasma described in section 4.1.

Table 3. NSTX: power flow to each species. The 'Reference' simulation corresponds to the original Maxwellian case while 'Numerical' simulation uses a numerically computed susceptibility χ_{D-NBI} (equation (11)) assuming a Maxwellian functional form of the representation of the distribution function.

Absorbed fraction	Reference	Numerical
D	0.22%	0.22%
D—NBI	73.88%	73.58%
Electrons	25.90%	26.21%

4.3.2. HHFW heating regime. As similarly done above, two series of computations assuming an anisotropic Maxwellian form for the fast ions (D-NBI) population in NSTX plasma have been performed. The fast ion absorption fraction, P_{D-NBI}, showed a significant variation when $C_\perp$ was varied from 0.5 to 5, with $C_\parallel$ held fixed at unity. In particular, for $C_\perp = \{0.5, 1., 3., 5.\}$, the corresponding $P_{D-NBI} = \{70.06, 73.56, 62.84, 48.48\}$. In contrast, when $C_\perp$ was fixed at unity and $C_\parallel$ was varied, P_{D-NBI}, varied by less than one percent. This behavior is the opposite with respect to what has been found in the IC minority heating regime. However, the absorption profile tends to be localized to the resonant layer for small $C_\parallel$ as shown in figure 8 in agreement with the results shown in the previous section. In this figure the absorption versus (R,Z) is shown for $C_\parallel = 0.5$ (figure 8(*a*)) $C_\parallel = 1.0$ (figure 8(*b*)), and $C_\parallel = 5.$ (figure 8(*c*)).

For the fast ion distributions in NSTX plasma, an additional application has been performed assuming a slowing down distribution function as described in the following section.

4.4. Slowing down distributions for beam ion species in HHFW heating regime

Another functional form of the distribution function for the beam ion species which has been implemented in the generalization of TORIC v.5 is a slowing-down distribution [32]

$$f_{D-NBI}(v) = \begin{cases} A\dfrac{1}{v_c^3}\dfrac{1}{1+(v/v_c)^3} & \text{for } v < v_m, \\ 0 & \text{for } v > v_m, \end{cases} \quad (20)$$

where $v = \sqrt{v_\parallel^2 + v_\perp^2}$ and $v_m \equiv \sqrt{2E_{D-NBI}/m_D}$ is the maximum velocity corresponding to the injected energy E_{D-NBI} of the beam ions. Also, $A = 3/[4\pi \ln(1 + \delta^{-3})]$ with $\delta \equiv \frac{v_c}{v_m}$, and

$v_c^3 = 3\sqrt{\pi}(m_e/m_D)Z_{eff}v_{th}^3$ where $Z_{eff} \equiv \sum_{ions} Z_i^2 n_i/n_e$. The fast ion absorption fraction, P_{D-NBI}, showed a significant variation when E_{D-NBI} was varied from 30 to 120 keV, with $Z_{eff} = 2$. In particular, for $E_{D-NBI} = \{30, 60, 90, 120\}$ keV, the corresponding $P_{D-NBI} = \{77.84, 75.85, 70.97, 64.71\}$. This result recalls the behavior found in bi-Maxwellian case when the parameter $C_\perp$ was varied indicating that the interaction between fast ions and fast waves occurs mainly in the perpendicular direction with respect to the magnetic field [1]. However, the absorption profile tends to be localized to the resonant layer for small E_{D-NBI} as shown in figure 9 in agreement with the results shown in the bi-Maxwellian case for both IC minority and HHFW heating regimes (see figures 7 and 8). In particular, figure 9 shows the power density versus (R, Z) for $E_{D-NBI} = 30$ keV (figure 9(*a*)), $E_{D-NBI} = 60$ keV (figure 9(*b*)), $E_{D-NBI} = 90$ keV (figure 9(*c*)), and $E_{D-NBI} = 120$ keV (figure 9(*d*)).

4.5. Numerical distributions

The main goal of this extension of TORIC is to enable the code to deal with (numerical) distribution functions provided by either Monte-Carlo particle or Fokker–Planck codes. In this section we describe our calculations by using (i) a distribution function obtained from the Fokker–Planck code CQL3D [3, 4] for an Alcator C-Mod plasma and (ii) a distribution function obtained from the Monte-Carlo particle code NUBEAM [29, 30] for an NSTX plasma.

4.5.1. IC minority heating regime. The TORIC extension can also utilize numerical distribution functions obtained from the Fokker–Planck code CQL3D for IC minority heating regime. This is a crucial step in ultimately closing the loop between RF and Fokker–Planck solvers and the evolution of the distribution of the H minority. Indeed, this will be shown in a future paper where a RF quasi-linear diffusion operator will be implemented in the TORIC code [33].

Figure 10 shows an example of distribution function of the H minority obtained from the iteration between the full wave code AORSA and the Fokker–Planck code CQL3D for Alcator C-Mod plasma [34, 35]. More specifically, figures 10(*a*) and (*b*) correspond to the distribution functions at 0th and 4th iteration, respectively. Both distribution functions are plotted at $\rho_{pol} = 0.2$. It is important to note that at 0th iteration the distribution function is a Maxwellian distribution (we refer to as 'Maxwellian case') while at the 4th iteration the RF tail is formed (see, four energy levels—10, 250, 500, and 1000 keV—for reference). We refer to this as 'non-Maxwellian case'. In order to evaluate the impact of the non-Maxwellian effects in the power deposition of the H minority, we compute numerically χ for both the numerical distributions shown in
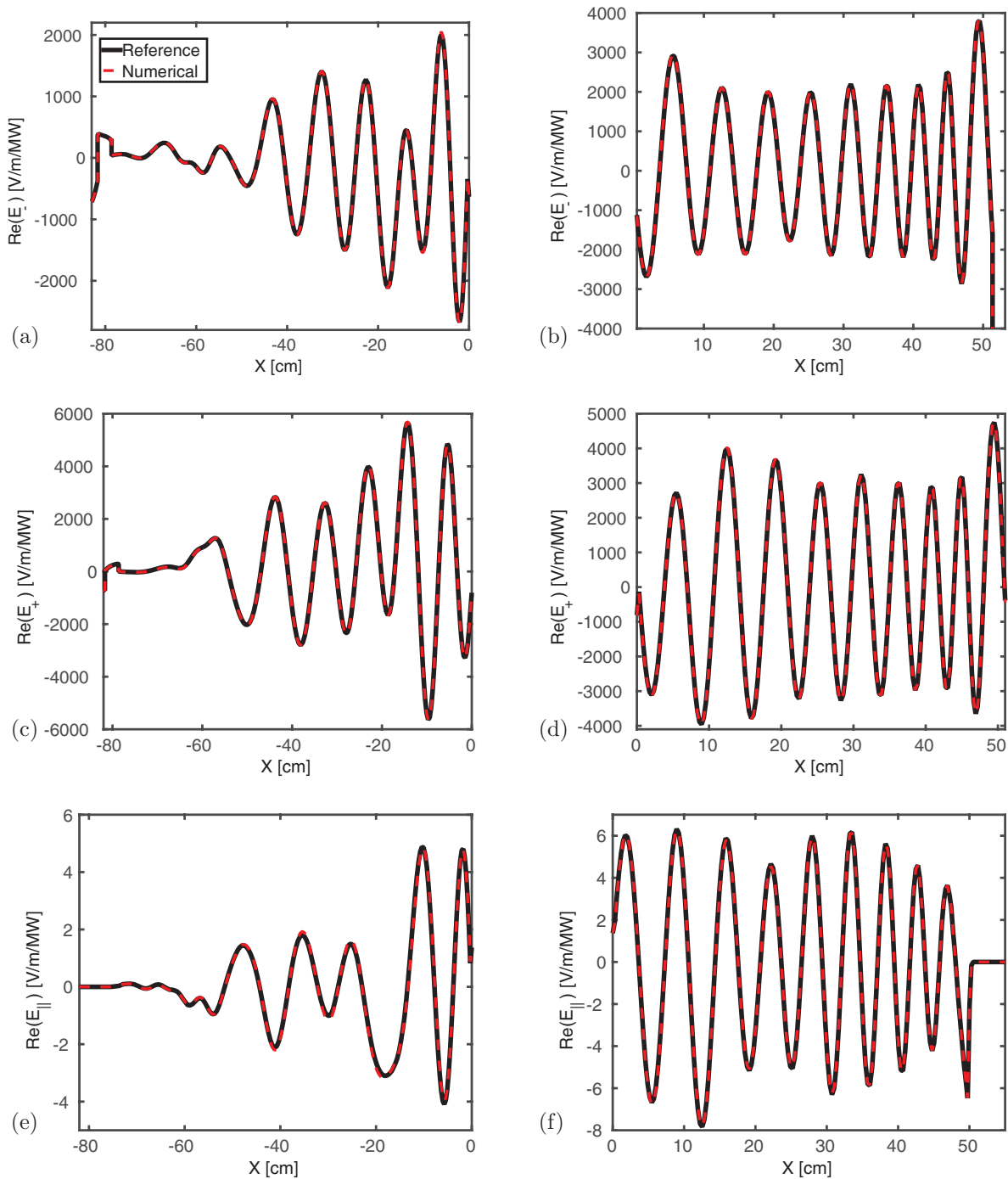
Figure 6. Figures (*a*) and (*b*): real part of the right-handed wave electric field, Re(E_-), both in the high field side region (figure (*a*)) and in the low field line region (figure (*b*)) on the midplane for an NSTX plasma described in section 4.1. The solid (black) curve represents the 'Reference' case while the dashed (red) curve represents the results re-computed with the susceptibility calculated numerically. Figures (*c*) and (*d*): real part of the left-handed wave electric field, Re(E_+), both in the high field side region (figure (*c*)) and in the low field line region (figure (*d*)). Figures (*e*) and (*f*): real part of the parallel wave electric field, Re($E_\parallel$), both in the high field side region (figure (*e*)) and in the low field line region (figure (*f*)).

figure 10 on a uniform numerical mesh of $N_{v_\parallel} = 500$ points and $N_{v_\perp} = 200$ points and the anisotropic Maxwellian distribution with the same energy content in the parallel and perpendicular directions as the actual distribution. The mesh range $-c/100 \leqslant v_\parallel \leqslant c/100$ and $0 \leqslant v_\perp \leqslant c/100$. Table 4 shows that the power flow to H minority increases when the RF tail at

higher energy is formed with respect to the Maxwellian case, both using the actual distribution function and the anisotropic Maxwellian distribution ('bi-Maxw' case). Furthermore, figure 11 shows the contour plot of the power density of the H minority for both the Maxwellian case (figure (*a*)) and the non-Maxwellian case (figure (*b*)). One can note that the
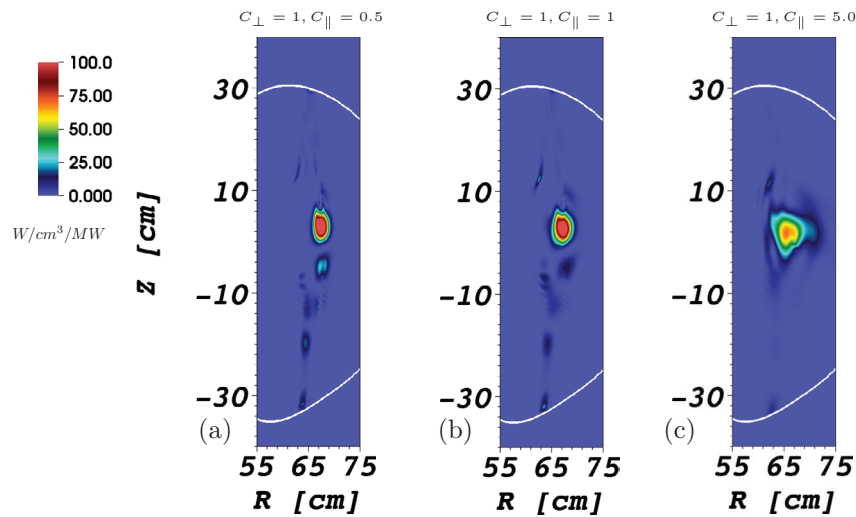
Figure 7. Contour plots of fundamental absorption by minority hydrogen (zoomed around the resonance), represented by a bi-Maxwellian distribution function (see equation (19)) in an Alcator C-Mod plasma for $C_\perp = 1.0$ and for $C_\parallel = 0.5$ (*a*), $C_\parallel = 1.0$ (*b*), and $C_\parallel = 5.0$ (*c*). The white curve represents the last closed flux surface. Units are Watts cm^{-3} at 1 MW incident power.
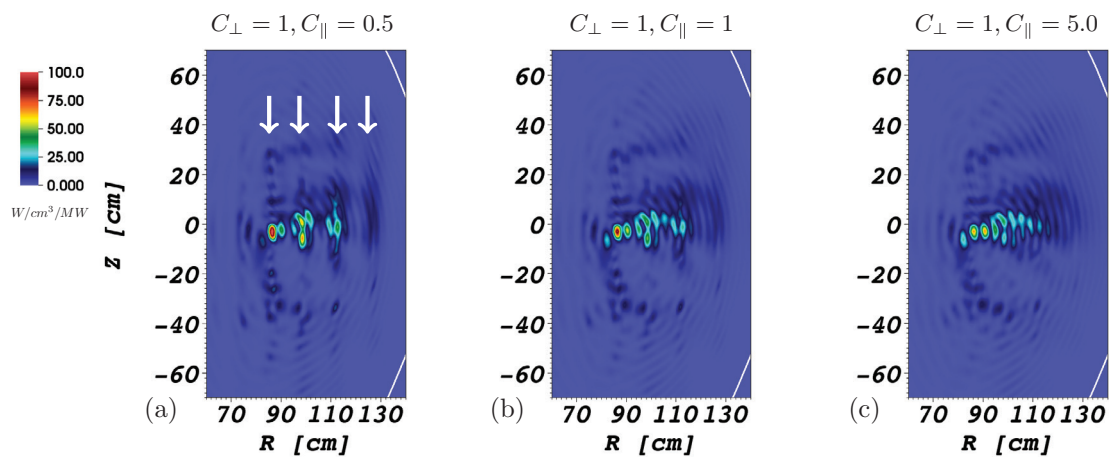

Figure 8. Contour plots of the absorption by beam ions (zoomed around the cyclotron resonances) represented by a bi-Maxwellian distribution function in an NSTX plasma for $C_\perp = 1.0$ and for $C_\parallel = 0.5$ (*a*), $C_\parallel = 1.0$ (*b*), and $C_\parallel = 5.0$ (*c*). The white curve represents the last closed flux surface. The white arrows in figure (*a*) indicate the deuterium cyclotron resonance layers ($n = 7, 8, 9$, and 10). Units are Watts cm^{-3} at 1 MW incident power.
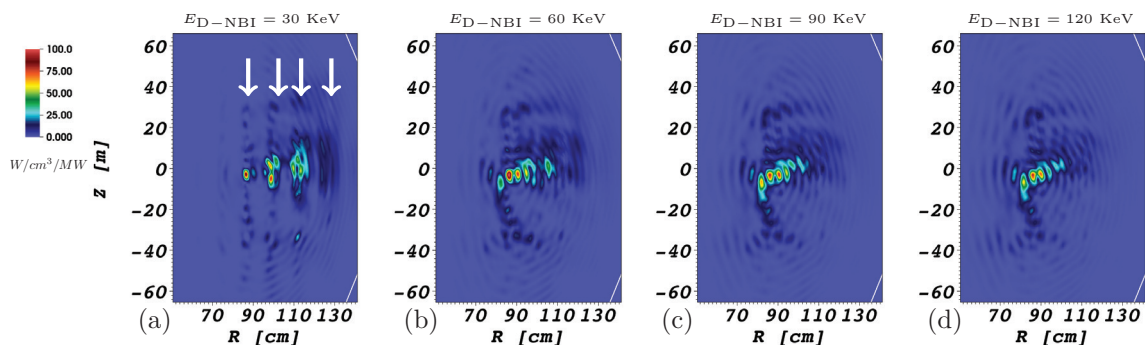
Figure 9. Contour plots of the absorption by beam ions represented by a slowing down distribution function (see equation (20)) in an NSTX plasma for different NBI injected energy E_{D-NBI} (shown in the plots). The white curve represents the last closed flux surface. The white arrows in figure (*a*) indicate the deuterium cyclotron resonance layers ($n = 7, 8, 9$, and 10).

non-Maxwellian effects tend to broaden the power deposition profile as clearly seen in figure (*b*). This result reflects what has been shown for a bi-Maxwellian by varying the parallel temperature (see figure 7).

4.5.2. HHFW heating regime. Besides the capability to deal with numerical distribution functions obtained from the Fokker–Planck code CQL3D for IC minority heating regime, the extension of TORIC is also able now to use directly the

(a)

(b)
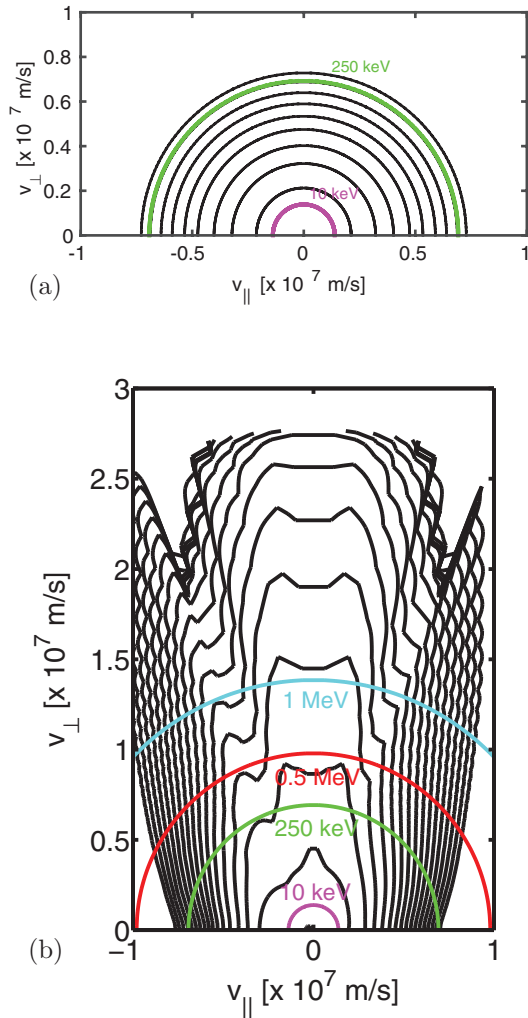
Figure 10. Minority H distribution function from the iteration between AORSA and CQL3D for Alcator C-Mod at $\rho_{pol} = 0.2$. Figures (*a*) and (*b*) show the distribution at 0th and 4th iteration respectively.

Table 4. Power flow to each species. The Maxw. case corresponds to the numerical Maxwellian distribution from CQL3D at step 0 while the Non-Maxw. case corresponds to the numerical non-Maxwellian distribution obtained by CQL3D after 4 iteractions (see figure 10 as an example). Finally, the bi-Maxw. case corresponds to the anisotropic Maxwellian (see equation (19)) with the same energy content in the parallel and perpendicular directions as the actual distribution for the 'non-Maxw' case.

Abs. fraction	Maxw.	Non-Maxw.	bi-Maxw.
2nd Harmonic D	18.38%	11.85%	15.86%
Fundamental H	58.82%	72.89%	67.83%
Electrons—FW	12.94%	9.40%	11.64%
Electrons—IBW	9.85%	5.86%	4.67%

particle lists generated by the Monte-Carlo particle code NUBEAM. This feature is particularly important for the study of the interaction between fast waves and energetic particles, such as fast ions generated by NBI as in NSTX [36].

Here the coupling of a particle based code (NUBEAM) with a continuum code (TORIC) is handled by P2F [37, 38]. The

P2F[5] code converts a discrete particle list to a 4-D continuum distribution function. The 4 dimensions are 2 cylindrical in space (R, z) and 2 cylindrical in velocity space ($v_\perp$, $v_\parallel$) with parallel being along the local B field direction of the corresponding spatial grid point. Conceptually P2F generates a histogram of the input particles in it's 4-D grid. However, since the full-wave code takes velocity space derivatives of the beam distribution function, that function must be smooth enough for the derivatives to be robust. This means that a box-function style histogram, even at 10^6 particles, produces a histogram where noise dominates the derivatives, especially at the larger velocities. To resolve this issue P2F implements two smoothing techniques. The first is a velocity space Gaussian particle shape with user defined width (see [38] for details), and the second is to distribute each computational particle along its unperturbed guiding center bounce orbit weighted according to time spent in each of the 4-D histogram bins. While the unperturbed orbit method results in robust velocity space derivatives, it will not reveal velocity space gradients sharper than those defined by the Gaussian particle width, i.e. we must choose the minimum Gaussian width necessary to ensure robustness of the velocity space derivatives for a particular number of computational particles, and also choose a number of computational particles in the NUBEAM calculation to ensure insensitivity of the resulting full-wave calculation to that number. In the work presented here we make use of both the two smoothing techniques implemented in P2F.

As done in the previous sections, to test our implementation we first check the Maxwellian distribution case by making use of the P2F code. First, we have artificially generated a particle list representing a Maxwellian distribution in an NSTX plasma geometry with analytical temperature and density profiles given by analytical kinetic profiles for electron and fast ion population. More specifically, the parameters were:

$$n_e(\rho_{pol} = 0) = 2.5 \times 10^{13} \, \text{cm}^{-3} \quad (21)$$

$$n_e(\rho_{pol} = 1) = 2.5 \times 10^{12} \, \text{cm}^{-3} \quad (22)$$

$$T_e(\rho_{pol} = 0) = 1\text{keV}; \, T_e(\rho_{pol} = 1) = 0.1 \, \text{keV} \quad (23)$$

$$n_{FI}(\rho_{pol} = 0) = 2.0 \times 10^{12} \, \text{cm}^{-3} \quad (24)$$

$$n_{FI}(\rho_{pol} = 1) = 2.0 \times 10^{11} \, \text{cm}^{-3}; \quad (25)$$

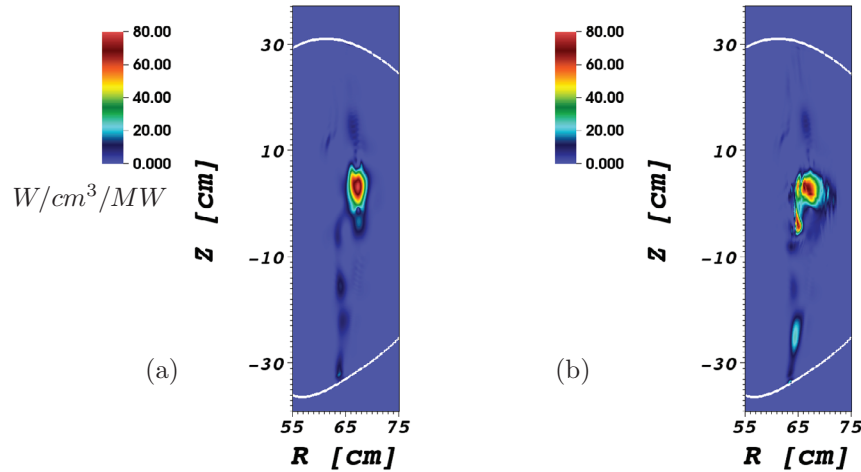with parabolic profiles and for the fast ion temperatures employed are given by

$$T_{FI}(\rho_{pol}) = (T_{FI,0} - T_{FI,1})(1 - \rho_{pol}^2)^5 + T_{FI,1} \quad (26)$$

with

$$T_{FI,0} \equiv T_{FI}(\rho_{pol} = 1) = 20 \, \text{keV}; \quad (27)$$

$$T_{FI,1} \equiv T_{FI}(\rho_{pol} = 1) = 5 \, \text{keV} \quad (28)$$

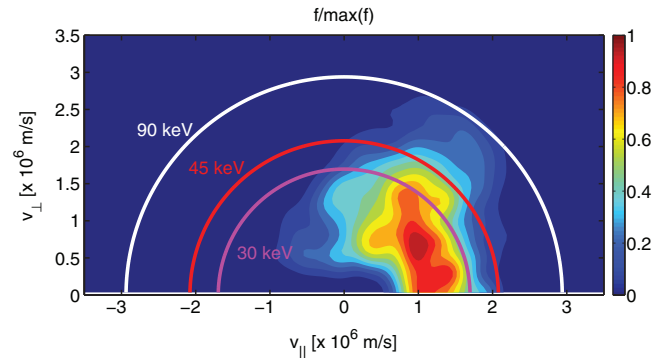[5] Available at https://github.com/ORNL-Fusion/p2f

Figure 11. H minority absorption profile from the `TORIC` solver for: (*a*) `CQL3D` Maxwellian case (initial step); (*b*) `CQL3D` non-Maxwellian case (final step).
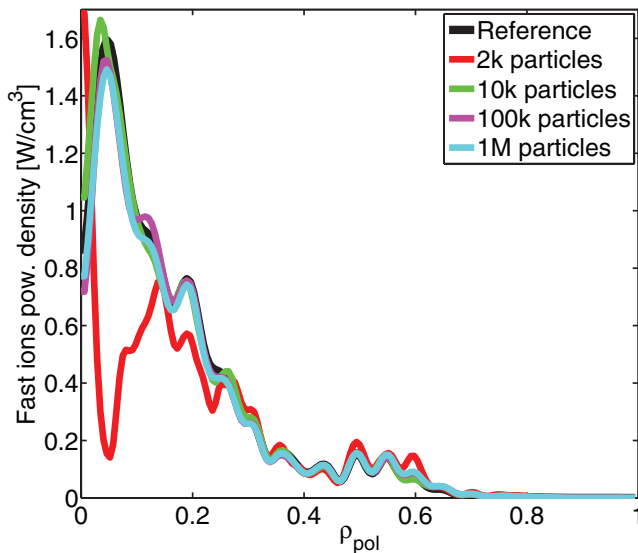
Figure 12. RF power deposition on fast ions from `TORIC` using `P2F` distributions as a function of ρ_{pol}. Black curve represents the reference case whereas the color curves indicate different particle number adopted in the calculations as shown in the legend.

Figure 13. Fast ion distribution function at $R = 1$ m and $z = 0$ m obtained from the `P2F` code starting from a `NUBEAM` particles list for an NSTX plasma without HHFW (shot 141 711 at time $= 0.47$ s).

Table 5. Power flow to each species. The Maxw. case corresponds to an equivalent Maxwellian temperature for the fast ions population (see equation (18)), the Non-Maxw. case corresponds to the numerical non-Maxwellian distribution obtained by `P2F` starting from a `NUBEAM` particles list. Finally, the bi-Maxw. case corresponds to the anisotropic Maxwellian (see equation (19)) with the same energy content in the parallel and perpendicular directions as the actual distribution.

Abs. fraction	Maxw.	Non-Maxw.	bi-Maxw.
D	4.26%	3.89%	10.27%
D-NBI	53.94%	58.12%	55.55%
Electrons	41.80%	37.99%	34.18%

Second, we have run `P2F` by using the Maxwellian particles list to obtain a continuum distribution function. Third, we have numerically evaluated χ and we have run `TORIC`. Finally, we have compared the results with the reference case. Figure 12 shows indeed the results of this comparison. In particular, in figure 12 the black curve indicates the reference case. In addition, there are other four cases which are obtained assuming a particles list with 2×10^3 (red curve), 10^4 (green), 10^5 (magenta curve), and 10^6 (cyan curve) particles. The numerical case converges to excellent agreement with the reference case as the number of particles is increased. It is also important to note two points: (i) the total power to the fast ions among the three cases with 10^4, 10^5, and 10^6 number of particles differs by less than 1%; (ii) good convergence is already achieved with 10^4 particles. This is an important point for the future application in time dependent modeling frameworks, such as TRANSP simulations. Finally, it is important to mention that, during the process to test P2F for a Maxwellian distribution function, particular attention have been given on the impact of the values of the Gaussian particle width comparing the input temperature profile adopted with the simulation (equations (26)–(28)) with the temperature profiles obtained from the distribution function calculated by P2F. Different values of Gaussian particle width marginally affect the lower energy tails of the temperature profile with respect to the input profile. Therefore, in the end, the Gaussian particle width was fixed to the value of 0.15 keV for all cases shown in figure 12. This value is very small with respect to the maximum temperature value, which is 20 keV (see equation (27)).
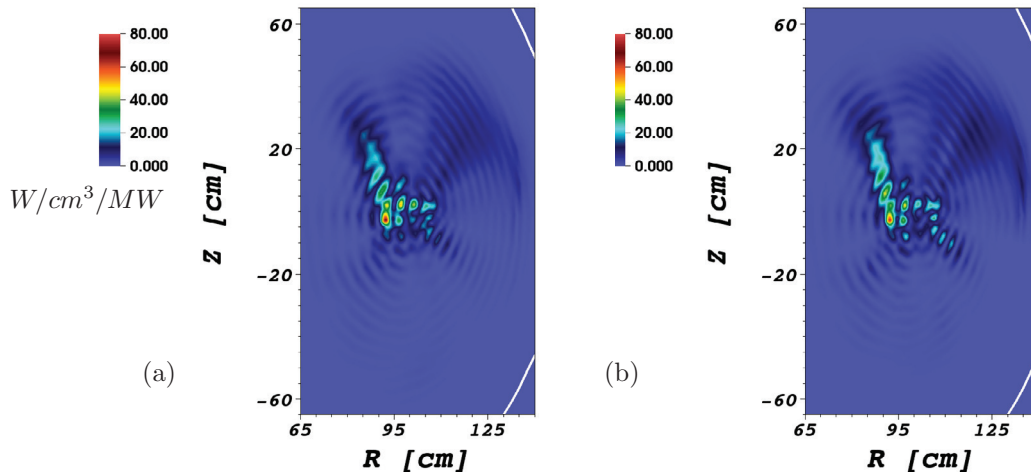
Figure 14. Fast ion absorption profile for: (*a*) equivalent Maxwellian case; (*b*) `NUBEAM` non-Maxwellian case.

Finally, figure 13 shows the fast ion distribution function at $R = 1$ m and $z = 0$ m obtained from the `P2F` code starting from a `NUBEAM` particles list for a NSTX shot 141 711 at time $= 0.47$ s without HHFW. The number of particles used for this case in `NUBEAM` are 531 15. For reference, the 90 keV beam injection energy is represented by the white curve while the half (45 keV) and third energy (30 keV) components are represented by red and magenta curves, respectively. As done for the minority heating regimes, power flow to the different species is shown in table 5. As expected, a larger power flow to fast ions is found when a realistic distribution is considered with respect to the equivalent Maxwellian case. It is worth noting that the relatively small differences in the power flow to fast ions between equivalent Maxwellian and the realistic case shown in table 5, are due to the fact that the distribution function in the case considered here is not affected by RF therefore the distribution function does not have a large RF tail to higher energies. Furthermore, in table 5 is shown the power flow to the fast ions for an anisotropic Maxwellian distribution (see equation (19)) with the same energy content in the parallel and perpendicular directions as the actual distribution shown in figure 13. Figure 14 shows the comparison of the equivalent Maxwellian distribution and the realistic distribution starting from `NUBEAM`, in terms of the 2D fast ion power density. For equivalent Maxwellian distribution we mean that we use an effective temperature of the beam ions temperature (T_{bi}) given by equation (18). From figure 14, one can only see a slight change (a slight broadening) in the profile when the realistic distribution is adopted although there is a variation in the power flow shown in table 5. The consideration of a realistic distribution obtained starting from `NUBEAM` and affected by RF, will be part of a future work which requires the study of a quasi-linear RF diffusion operator (also called RF kick operator) in `NUBEAM`. In this scenario, we might expect a larger amount of power deposited to the fast ions population due to a larger distribution function tail formed by the RF application. This could have a strong impact in the recent NSTX experimental observations where HHFW was able to fully suppress Alfvén activities, such as Toroial Alfvén Eigenmodes (TAEs) and Global Alfvén Eigenmodes (GAEs) [39].

5. Conclusions

The ICRF wave simulation code `TORIC` has been generalized to allow prescription of arbitrary particle distribution functions of the form $f(v_{\parallel}, v_{\perp}, \theta, \psi)$ in the computation of the plasma susceptibility in both the minority and HHFW heating regimes. The algorithm was validated by recovering results for RF heating in Alcator C-MOD and NSTX obtained by computing χ using analytic approximations to the plasma dispersion function for the case when all species are Maxwellian. The application of bi-Maxwellian distribution function shows a different behavior in the total absorbed power between the most common IC minority and HHFW heating regimes. In particular, for IC minority heating regime, the total absorbed power at the H fundamental is insensitive to variations in the perpendicular temperature ($T_{\perp}$), but varies with changes in parallel temperature ($T_{\parallel}$), whereas for HHFW regime, the behavior is reversed, namely, the total absorbed power by fast ions is insensitive to variations in $T_{\parallel}$, thus reflecting the well-known Doppler broadening effect of parallel temperature on the absorption profile. However, for both heating regimes, the power density profiles vary with changes in $T_{\parallel}$. Similar results have been found and shown for HHFW heating regime assuming a slowing-down distribution function. The impact of the non-Maxwellian effects with respect to the Maxwellian case has been evaluated in both IC minority heating regime by using a distribution function obtained from a Fokker–Planck code `CQL3D` and HHFW heating regime by using a distribution function obtained from the Monte-Carlo particle code `NUBEAM`. Both cases indicate that the use of a realistic distribution function tends to increase the power flow to the H for the minority heating and to the fast ions for the HHFW heating regime.

This work represents a first step towards closing the loop between the extension of `TORIC` in a self-consistent way and the `CQL3D` code for the IC minority heating regime as used, for instance, in Alcator C-MOD experiments and the `NUBEAM` code for HHFW heating regime as used in NSTX-U experiment. This work is done with the aim to be able to make time dependent simulations in TRANSP in a self-consistent way.

Work on the quasilinear diffusion coefficients for the finite Larmor radius (FLR) approximation (valid for the IC minority regimes) and on the RF kick-operator in `NUBEAM` are in progress and the results will be presented in a future paper.

Acknowledgments

References

[1] Stix T.H. 1975 *Nucl. Fusion* **15** 737
[2] Jaeger E.F. *et al* 2001 *Phys. Plasmas* **8** 1573
[3] Harvey R.W. and McCoy M.G. 1992 The CQL3D Code *Proc. IAEA TCM on Advances in Sim. and Modeling of Thermonuclear Plasmas (Montreal, 1992)* pp 489–526 (available through USDOC/NTIS No. DE93002962; see also www.compxco.com/cql3d.html CQL3D Manual)
[4] Petrov Y.V. and Harvey R.W. 2016 *Plasma Phys. Control. Fusion* **58** 115001
[5] Jaeger E.F. *et al* 2006 *Phys. Plasmas* **13** 056101
[6] Smithe D. 1989 *Plasma Phys. Control. Fusion* **31** 1105
[7] Dumont R.J. 2005 *Phys. Plasmas* **12** 042508
[8] Murakami S. *et al* 2006 *Nucl. Fusion* **46** S425
[9] Brambilla M. and Bilato R. 2009 *Nucl. Fusion* **49** 085004
[10] Bilato R. *et al* 2011 *Nucl. Fusion* **51** 103034
[11] Lerche E. *et al* 2009 *Plasma Phys. Control. Fusion* **51** 044006
[12] Choi M. *et al* 2010 *Phys. Plasmas* **17** 056102
[13] Jucker M. *et al* 2011 *Comput. Phys. Commun.* **182** 912
[14] Dumont R.J. 2009 *Nucl. Fusion* **49** 075033
[15] Dumont R.J. and Zarzoso D. 2013 *Nucl. Fusion* **53** 013002
[16] Hellsten T. *et al* 2013 *Nucl. Fusion* **53** 093004
[17] Brambilla M. 1999 *Plasma Phys. Control. Fusion* **41** 1
[18] Brambilla M. 2002 *Plasma Phys. Control. Fusion* **44** 2423
[19] Hawryluk R.J. 1980 *Physics Close to Thermonuclear Conditions* vol 1 ed B. Coppi *et al* (Brussels: Commission of the European Communities) p 19
[20] Bonoli P.T. *et al* 1999 *Phys. Plasmas* **7** 1886
[21] Kaye S.M. 2015 *Nucl. Fusion* **55** 104002
[22] Brambilla M. 1996 *Technical Report* No IPP 5/66 Max Planck Institute fuer Plasmaphysik
[23] Phillips C.K. *et al* 2003 *AIP Conf. Proc.* **694** 499
[24] Stix T.H. 1992 *Waves in Plasmas* (New York: American Institute of Physics)
[25] Fried B.D. and Conte S.D. 1961 *The Plasma Dispersion Function* (New York: Academic)
[26] Wright J.C. *et al* 2008 *Commun. Comput. Phys.* **4** 545
[27] Bilato R. *et al* 2014 *Adv. Comput. Math.* **40** 1159
[28] Bertelli N. *et al* 2014 *AIP Conf. Proc.* **1580** 310
[29] Goldston R.J. *et al* 1981 *J. Comput. Phys.* **43** 61
[30] Pankin A. *et al* 2004 *Comput. Phys. Commun.* **159** 157
[31] Eriksson L.G. and Helander P. 1994 *Phys. Plasmas* **1** 308
[32] Batchelor D.B., Jaeger E.F. and Colestock P.L. 1989 *Phys. Fluids* B **1** 1174
[33] Lee J.P. *et al* 2015 *Bull Am. Phys. Soc.* **60** 242; 2017 *Phys. Plasmas* submitted
[34] Bader A. 2011 Experimental measurements and numerical modeling of fast-ion distributions on the Alcator C-Mod tokamak *PhD Thesis* MIT, Department of Nuclear Science and Engineering
[35] Bader A. *et al* 2012 *Nucl. Fusion* **52** 094019
[36] Rosenberg A.L. *et al* 2004 *Phys. Plasmas* **11** 2441
[37] Green D.L. *et al* 2009 *J. Phys.: Conf. Ser.* **180** 012058
[38] Green D.L. *et al* 2009 *AIP Conf. Proc.* **1187** 569
[39] Fredrickson E.D. *et al* 2015 *Nucl. Fusion* **55** 013012